Bulk crystal growth and surface preparation of NiSb, MnSb, and NiMnSb

Ian Maskery,[a] Christopher W. Burrows, Marc Walker, Ravi P. Singh,[b] Geetha Balakrishnan,
Jon A. Duffy, and Gavin R. Bell[c]
Department of Physics, University of Warwick, Coventry CV4 7AL, United Kingdom

Bulk single crystal and polycrystalline samples of NiSb, MnSb, and NiMnSb have been grown and characterized. The lattice parameter of NiMnSb was found to be 5.945 ± 0.001 Å, around 0.25% larger than previous reports. The surface preparation of these materials was investigated using x-ray photoelectron spectroscopy. Wet etching with HCl and argon ion sputtering were used in tandem with vacuum annealing. For both binary materials, a clean and stoichiometric surface could be regained by HCl etching and annealing alone. However, clean and stoichiometric ternary NiMnSb was not successfully prepared by these methods. The transition metal 2p and 3p levels are analyzed for all three materials. © 2016 Author(s). All article content, except where otherwise noted, is licensed under a Creative Commons Attribution (CC BY) license (*http://creativecommons.org/licenses/by/4.0/*). [http://dx.doi.org/10.1116/1.4953549]

I. INTRODUCTION

The experimental[1–7] and theoretical[8–16] study of half-metallic ferromagnetic (HMF) materials continues among many groups, motivated by both fundamental interest in the unusual electronic structure of this class of materials and their potential for use in spintronic and magnetoelectronic devices. The high Fermi level spin polarization (P_{DOS}) of HMFs is a great advantage: in principle, $P_{DOS} = 100\%$ for an HMF material, although several factors can corrupt ideal half-metallicity. Even for stoichiometric single-crystal material, nonzero temperature, atomic-scale disorder and altered local atomic environments at interfaces[13–17] can all result in a loss of spin polarization. Half-metallicity was first proposed in NiMnSb by de Groot and Mueller using electronic structure calculations.[18] Since then many studies, using mainly density functional theory (DFT) at $T = 0$ K, have been undertaken. Such work has explored HMF behavior in materials as diverse as Heusler alloys,[15,19] half-Heusler alloys,[8,14] zincblende-structure binary transition metal pnictides[16,20,21] and chalcogenides,[22,23] transition metal oxides,[13] complex oxides,[24] carbides,[10] nitrides,[11] selenides,[25] and porphyrins.[26] Some theoretical studies have also investigated finite-temperature band structure and spin polarization beyond standard DFT.[8,20,27–29] All of these valuable theoretical studies should be compared to experimental data, which places stringent demands on both material production and analysis techniques.

Atomic-scale disorder and nonstoichiometry in the bulk and surface or interface reconstruction or relaxation of atomic structure can both affect P_{DOS}. This is, of course, critical for devices involving spin injection and detection in nonmagnetic semiconductor structures via HMF contacts and for superlattice-type spin filtering and spin–diode structures. However, these effects are also important in experimental determination of P_{DOS} since many experimental techniques either form an interface (e.g., point contact Andreev reflection[30]) or require a free surface (e.g., spin-polarized electron spectroscopies[2,31]). The sensitivity of reported spin polarizations to the experimental technique and the quality of the HMF material is reflected in the literature, especially for NiMnSb which has been studied since the 1980s, where there is wide variation in the reported value of spin polarization.[32–34] On the other hand, some experimental techniques sensitive to P_{DOS} require *bulk* rather than thin film samples (e.g., magnetic Compton scattering[35,36]). Therefore, high quality bulk crystals are also valuable in fundamental investigations of half-metallicity.

Several approaches to surface preparation of pnictides are available, including chemical etching,[37] ion bombardment and annealing (IBA), and atomic hydrogen cleaning (AHC).[38] A potential undesirable effect due to IBA is patterning or nanostructuring of surfaces.[39] Wet chemical methods can avoid near-surface damaged layers associated with sputtering. It is also worth noting that the practical applicability of a given HMF material can be enhanced by a suitable wet chemical etch for device processing.

In this paper, we examine the surface preparation of bulk samples of the ternary compound NiMnSb and its binary relations NiSb and MnSb, using HCl etching and IBA. NiMnSb has predicted minority spin gap $E_{gap} = 0.5$ eV at room temperature, with corresponding $P_{DOS} = 100\%$. However, nonzero temperature DFT using the disordered local moments approach suggests that even small reductions in magnetization will rapidly reduce the polarization due to defectlike states infecting the minority spin gap.[20] In contrast, MnSb is a weakly metallic ferrimagnetic compound with high Curie temperature, 587 K, and low predicted $P_{DOS} \approx 18\%$. Nonetheless due to its good interfacial properties, high magneto-optic Kerr rotation, strong transport spin polarization, and ease of chemical etching with dilute HCl,[37] it has proved useful in magnetoelectronic and optoelectronic applications,[40,41] The cubic polymorph of MnSb, which can be grown epitaxially, is predicted to be a much more robust HMF material than NiMnSb, with $E_{gap} = 1.0$ eV, far stronger resistance to magnetization

reduction[20] and promising interface structures.[16] Thin film growth of MnSb is fully compatible with many conventional III–V semiconductor materials. It also has applications in Li ion storage batteries.[42]

NiSb is a weakly metallic paramagnetic material which occurs naturally as the mineral breithauptite. It could be used as a spacer material in all-epitaxial multimagnetic structures,[43] e.g., based on the MnSb–CrSb–NiSb series. NiSb also has numerous potential applications in nanocomposite materials: recently, there has been a surge of interest in this family of materials for Li batteries.[44–49] Nanoparticle NiSb has potential as a heterogeneous catalyst[50] and has been investigated within an InSb matrix for thermoelectric applications.[51] For catalysis and battery anode applications, the surface properties are clearly critical.

In the present work, we show that the surfaces of NiSb and MnSb bulk samples could be prepared, after polishing and air exposure, by wet etching in HCl and subsequent vacuum annealing. We also demonstrate growth of high quality NiMnSb single crystals and investigate the preparation of NiMnSb surfaces. However, in contrast to its binary relations, a clean stoichiometric surface of NiMnSb could not be prepared by procedures using HCl wet etching, sputtering with Ar ions and vacuum annealing.

II. EXPERIMENTAL DETAILS

A. Bulk crystal growth and stoichiometry

Polycrystalline samples of NiSb, MnSb, and NiMnSb were prepared by arc melting high purity (99.99% or better) powders of Ni, Mn, and Sb on a water cooled copper hearth under a high purity (5N) argon gas atmosphere in a tri-arc furnace (Centorr, USA). To ensure phase homogeneity, the resulting buttons were flipped and remelted several times. The arc melted samples were subsequently sealed in evacuated quartz tubes and annealed for 150 h. The annealing temperatures were 850 °C for NiMnSb and 800 °C for the binary compounds.[30] The resulting polycrystalline boules were around 7 mm in diameter. A larger ingot of NiMnSb was cast for crystal growth by the Czochralski method using a tetra-arc furnace (Cyberstar). A tungsten rod was used as a seed, and the growth was performed at 10 mm/h in an argon atmosphere. The NiMnSb crystal produced was around 20 mm long and 3 mm in diameter. A portion of the crystal boule was cut from the middle section into disks 2 mm thick for the measurements.

Samples were analyzed by energy dispersive x-ray analysis (EDX) using a Zeiss SUPRA55VP scanning electron microscope with EDAX Genesis analytical system, including standard corrections for atomic number, absorption, and fluorescence. Measurements on five different slices of a NiMnSb boule gave stoichiometry variations within ±0.5%. Optimization of the bulk stoichiometry is discussed in Sec. III A. Samples were also characterized by powder x-ray diffraction at room temperature using a Panalytical X-Pert Pro MPD K$_{\alpha 1}$ system. Single crystal samples were oriented crystallographically by x-ray Laue back-reflection.

B. Surface preparation and XPS analysis

Polished surfaces were prepared after first cutting sections from polycrystalline or single crystal ingots with a rotating diamond blade. After polishing to a mirror finish with increasingly fine grades of lapping paper, a final polish with a suspension of 0.25 µm diamond grit was used. Polished samples were cleaned ultrasonically in acetone then isopropanol then deionized water. The polished surfaces were imaged with reflected-light differential interference contrast (DIC) microscopy and atomic force microscopy (AFM) using an Asylum Research MFP-3D in tapping mode.

Before introduction into the ultrahigh vacuum (UHV) system, the samples were mounted on standard carrier plates or stubs using either spot-welded Ta wire or silver epoxy glue. Samples were etched in HCl (36% solution) for 10 s at room temperature then rinsed in deionized water and blown dry with nitrogen immediately before loading into vacuum; a longer etch of 30 s was also performed for NiMnSb. The fast-entry chamber was flushed continually with dry nitrogen before pumping down. One of the NiMnSb samples was also studied with only *in vacuo* surface cleaning and no prior HCl etch. Samples were annealed in UHV to either 250 or 300 °C in 1 h steps, except for a final long anneal for etched and sputtered NiMnSb. Argon ion sputtering conditions were: ion energy 500 eV or 1 keV, sample drain current around 1 µA, and polar angle of incidence 45°.

Sample surfaces were analyzed in UHV by x-ray photoelectron spectroscopy (XPS) using two systems equipped with monochromatic Al Kα sources (Omicron GmbH, Kratos Axis Ultra DLD) and base pressures 1×10^{-10} mbar. All the XPS experiments were performed at 90° take-off angle. In the Omicron system, the analyzer entrance slits were set to accept electrons from an area of the sample approximately 1.0 mm across. The corresponding analysis area in the Kratos system was approximately 0.3 × 0.7 mm. Data were obtained immediately after loading and then after different *in situ* surface treatments. Survey scans and detailed region scans were obtained at each stage. The Sb 3d region coincides with O 1s and so the Sb 4d shallow-core level was examined. Ni and Mn were studied through their 2p regions and shallow-core 3p levels. The C 1s and Cl 2p were recorded to monitor residual surface contamination. Detailed fitting of transition metal peaks can be challenging and due to the uncertainties associated with quantification of, e.g., Ni 2p in the absence of robust standards,[52] quantification of stoichiometry was performed here via peak analysis with standard relative sensitivity factors. Stoichiometry trends across samples subject to different treatments should be self-consistent, but absolute stoichiometries cannot be accurately claimed by this XPS analysis. More detailed peak fitting was performed on the Sb 4d peaks, with standard Shirley background and Voigt line shapes, in order to extract the fraction of oxidized Sb. The inelastic mean free path (IMFP) of photoelectrons was not included in the quantification. Instead a direct comparison was made between stoichiometry derived from the shallow-core lines (high electron kinetic energy, so higher IMFP) and Sb 3d/metal 2p lines

(lower electron kinetic energy hence lower IMFP). These are labeled "bulk" and "surface," respectively, but these labels are merely an indicator of the relative depth sensitivity of the measurement.

III. RESULTS AND DISCUSSION

A. Bulk stoichiometry optimization

The high vapor pressure of Sb means that an initially nonstoichiometric mix of source materials may be expected for optimum bulk crystal growth, to account for small nonstoichiometric losses at the tri-arc melting stage. In order to optimize this first step, several small binary and ternary polycrystal samples were grown with varying initial compositions. The composition after remelting stages was then checked with EDX. For the binary materials, an initially stoichiometric mix of materials indeed gave polycrystals with composition close to $M_{0.55}Sb_{0.45}$ (where M is Ni or Mn). A few percent excess Sb allowed polycrystals to be grown with elemental abundances equal to within $\pm 1\%$. The precise excess required depended on the number of remelting cycles performed since some Sb was lost at each stage. Because the Sb loss does not occur quite uniformly from one melting cycle to another, some trial and error is needed to grow stoichiometric material. All the subsequent surface preparation work was performed on stoichiometric MnSb and NiSb samples.

The ternary material behaved slightly differently, requiring a small excess of Mn to produce polycrystalline ingots close to stoichiometry. Similar behavior was reported by Gardelis[30] and Wang *et al.*:[3] both groups found some NiSb phase present in their NiMnSb polycrystalline samples, the amount of which was reduced by including a few percent excess of Mn. Our polycrystalline boules prepared with an initial 5% excess Mn were used for single crystal growth as described above. Example EDX data are shown in Fig. 1 for a NiMnSb single crystal slice after polishing and ultrasonic cleaning. Discounting about 2% residual surface contamination, the mean Ni:Mn:Sb composition ratios across five

different slices were found to be Ni 35.2%, Mn 32.3%, Sb 32.5%, varying by $\pm 0.5\%$.

B. NiMnSb single crystal and binary polycrystals

Figure 2 shows a photograph of some typical samples. A circular NiMnSb single crystal slice mounted on a UHV sample plate is in the center (b) flanked by larger polycrystalline NiSb (a) and MnSb (c) samples. The expected crystal structures were obtained for all three compounds, with no extraneous structures present. Example XRD data are shown in Fig. 3 for NiMnSb together with a calculation of the diffractogram. All of the expected peaks for the $C1_b$ structure of NiMnSb are present and close to the predicted intensity ratios, while no peaks due to extraneous phases[3,30] are present (calculated diffractograms for NiSb and MnSb are shown). The lattice parameter of NiMnSb was found to be 5.945 ± 0.001 Å. This is about 0.25% greater than previously reported values,[53,54] and 0.15% to 0.4% larger than the range reported by Gardelis[30] for polycrystalline NiMnSb with some NiSb phase present. The crystallographic orientation of our single crystal NiMnSb was confirmed to be $\langle 001 \rangle$ parallel to the main boule growth direction. A typical x-ray Laue image is shown in Fig. 4 obtained from a polished surface cut perpendicular to the growth direction. The clear fourfold symmetry is consistent with an {001} surface orientation.

The surface topography of the NiMnSb after two polishing steps is shown in the AFM images of Fig. 5. Image (a) is after the initial polish, and is dominated by scratches several tens of nm deep with small islandlike features typically 5–15 nm in height. The overall root-mean-square (RMS) roughness on this scale is around 3 nm. After the fine diamond grit polish (b), scratches are less evident, and the RMS roughness is only 2.5 nm even on this larger image. In general, one expects the measured RMS roughness to increase with image size, proportional to image size raised to an exponent β. The scaling of RMS roughness with image size
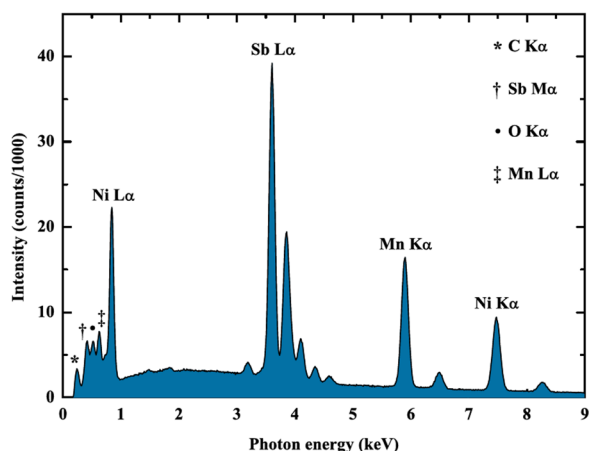

FIG. 1. (Color online) Sample EDX spectrum from stoichiometric single crystal NiMnSb after polishing and ultrasonic cleaning. The major Ni, Mn, and Sb peaks are identified directly, with low-energy peaks (<1 keV) labeled by symbols.
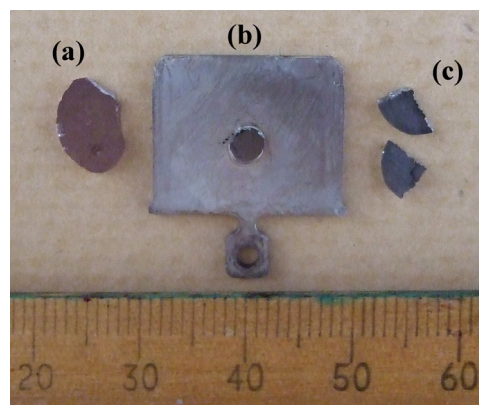

FIG. 2. (Color online) Photograph of a selection of samples. (a) Polycrystalline NiSb sample after polishing. (b) Single crystal NiMnSb polished and mounted on a standard UHV sample plate. Note that this sample is glued with UHV silver epoxy whereas standard samples for etching and XPS were mounted with spot-welded Ta wire. (c) Polycrystalline MnSb samples before polishing. The mirror finish of the polished samples is not obvious in the photograph but the characteristic pink hue of the NiSb is apparent.
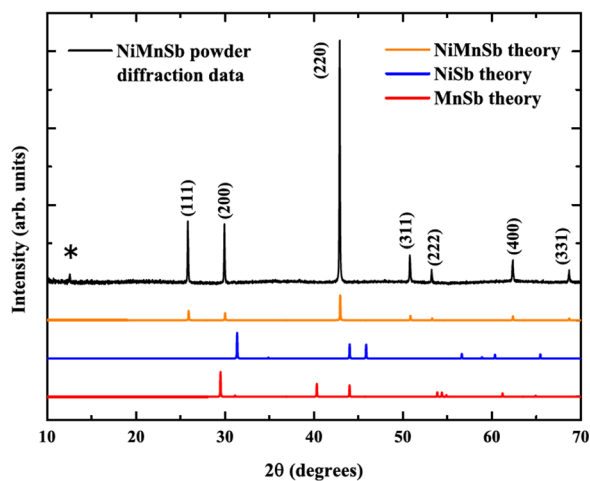
FIG. 3. (Color online) NiMnSb powder XRD. The black curve (uppermost) shows typical experimental data. The peaks are all readily indexed to NiMnSb; the weak peak at low angle labeled with an asterisk is due to the Al sample holder. Below the experimental data is shown a simulation (yellow curve) for pure NiMnSb giving excellent agreement with experiment. The two curves below are simulations for NiSb (blue, middle) and MnSb (red, bottom): these peaks are completely absent from experimental data.

is illustrated in Fig. 6 for NiMnSb before and after polishing. Prior to the final polish, the data are well fitted with $\beta = 0.60$, while $\beta = 0.34$ after the fine polish. This is consistent with the deeper polishing scratches being removed by the final polish and the overall variance of scratch depth reducing significantly. Prior to this, the increased likelihood of finding deep scratches on larger images keeps the exponent β high.

We also show some typical data for NiSb. In Fig. 5(c) is shown a typical DIC micrograph for polished NiSb. The colors represent phase contrast due to differently oriented grains. The grain size varies from several millimeters (e.g., the top left grain on the image extends much further) to $\sim 100 \, \mu m$. A corresponding AFM image is shown in Fig. 5(d). Long parallel polishing marks are evident along with islandlike features and pits. The RMS roughness is 8 nm, the
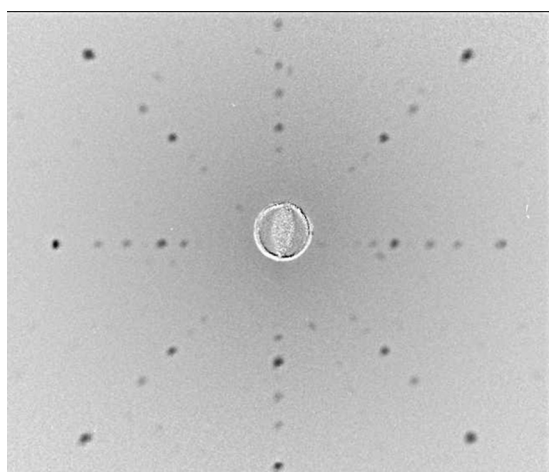

FIG. 4. X-ray Laue photograph of the NiMnSb crystal shown in Fig. 1(b) taken perpendicular to the polished (001) face.

smaller islands are typically 10 nm high and the pits several tens of nm deep (up to ~ 100 nm). The persistence of pits in the polycrystalline samples prevented them being polished as smoothly as the single crystal NiMnSb. The elongation of the small islands from bottom left to top right of the image is not a tip artifact since differently oriented features appear in different regions of the sample; rather, it seems to be a product of the polishing process. Pits were typically larger on the MnSb sample compared to NiSb giving correspondingly higher surface roughness.

C. Chemical cleaning of NiSb and MnSb

The binary compounds were studied by XPS in three states: untreated, after acid etching and after etching and a vacuum anneal. The survey spectra contained peaks due to Mn or Ni, Sb, O, C, and (after etching) Cl. Figures 7 and 8 show summaries of the XPS data for MnSb and NiSb, respectively, focusing on the metal 2p lines, Sb 4d shallow core levels and Sb 3d/O 1s region. Panels (g), (h), and (i) show the Sb 4d doublet. For clarity, detailed fits are not shown for MnSb and NiSb (the NiMnSb data presented later include example peak fits).

For MnSb, before surface treatment, the Sb 4d line appears as four overlapping peaks [Fig. 7(g)]. Etching immediately reduces the broader, higher binding energy components [Fig. 7(h)] and they have almost vanished after vacuum annealing [Fig. 7(i)]. These peaks were readily fitted as the Sb 4d doublet at around 32 eV with additional broader peaks at higher binding energy which can be assigned to Sb oxide. Table I gives the proportion of intensity in the Sb 4d oxide peaks compared to the MnSb-related peaks as a function of surface preparation stage. For NiSb, the progression is slightly different, with the Sb oxide peaks enhanced by the initial etch [Figs. 8(g)–8(h)]. However, the volatile Sb oxides are removed effectively by the vacuum anneal [Fig. 6(i)], leaving a nearly pure Sb 4d doublet. The oxide contribution after etching and annealing is 6% (NiSb) or 3% (MnSb). At low binding energy (high kinetic energy), the IMFP of electrons is relatively long, and so, this shallow core level signal has a strong contribution from subsurface Sb.

The center panels [(d)–(f)] in each figure show the overlapping O 1s and Sb 3d regions, for which the IMFP is somewhat shorter, giving higher surface specificity. Initially, there is a strong and quite broad O 1s peak in both spectra [Figs. 7 and 8(d)]. The Sb 3d doublet also has strong chemically shifted components at higher binding energy, due to the surface oxide. For MnSb, the etch strongly suppresses the O 1s peak and oxide peaks [Fig. 7(e)]. For NiSb, in agreement with the Sb 4d results, the O signal and Sb 3d chemically shifted component are both increased by the etch [Fig. 8(e)]. It is evident for both NiSb [Fig. 8(f)] and MnSb [Fig. 7(f)] that after etching and annealing the region comprises only the Sb 3d doublet with very little contribution from Sb oxides or O 1s. This is in agreement with the Sb 4d results but also indicates that the amount of O in the form of Ni or Mn oxides is similarly small.
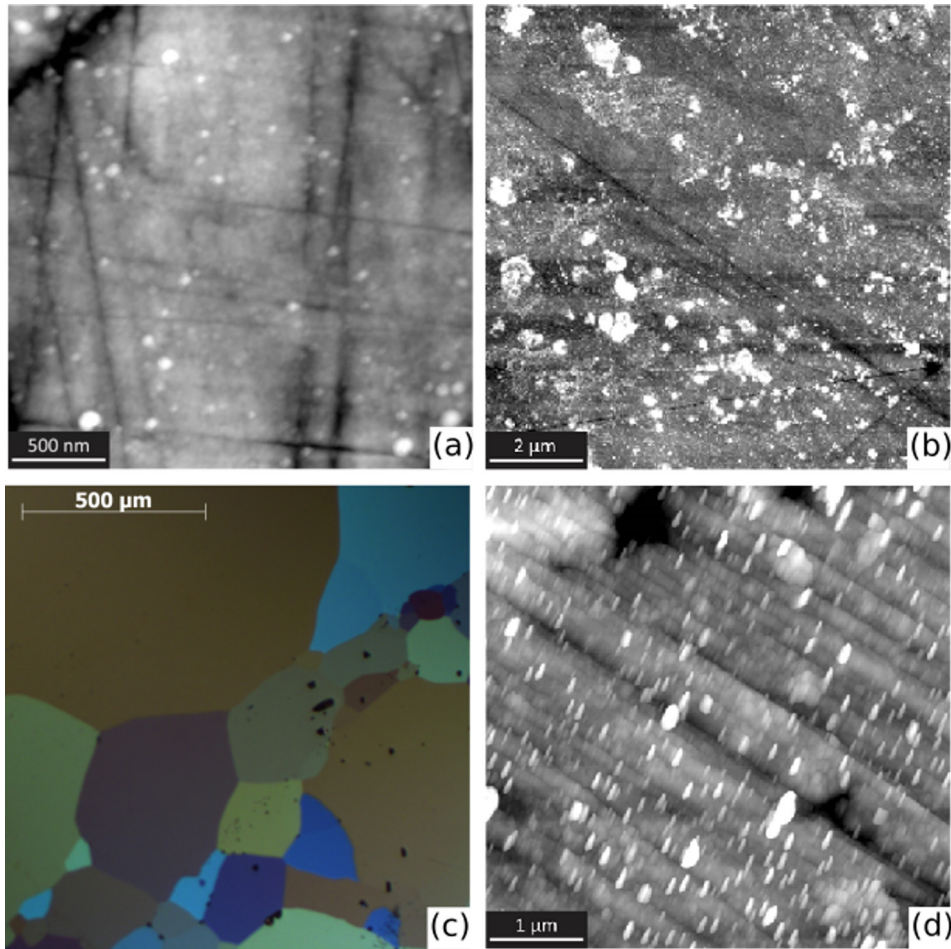
FIG. 5. (Color online) Selected microscopy data for NiMnSb and NiSb single crystals. AFM data for NiMnSb bulk crystal are shown after the initial polishing stage (a) and after final diamond grit polish (b). For NiSb, we show a typical IC micrograph (c) highlighting the grain structure of the polycrystal, and an AFM image after polishing (d).

The greater complexity[55] of the Mn and Ni 2p regions [Figs. 7 and 8(a)–8(c)] means that it is more difficult to assign simple oxide peaks. For NiSb, the etch appears to increase the intensity of a component with binding energy
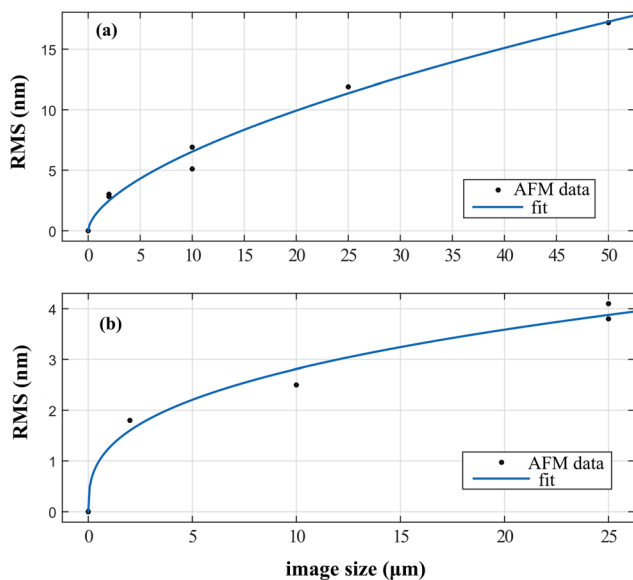

FIG. 6. (Color online) RMS roughness as a function of AFM image size for NiMnSb before (a) and after (b) the final polishing step. The fits are described in the text.

FIG. 7. XPS data for MnSb after different treatments: top row untreated, middle row after wet etching with HCl, and bottom row after subsequent vacuum annealing. The Mn 2p, Sb 3d, O 1s, and Sb 4d regions are shown.

JVST B - Nanotechnology and Microelectronics: Materials, Processing, Measurement, and Phenomena
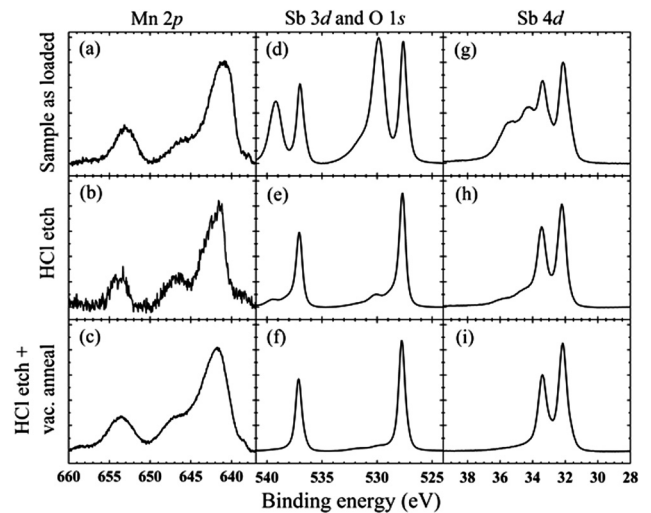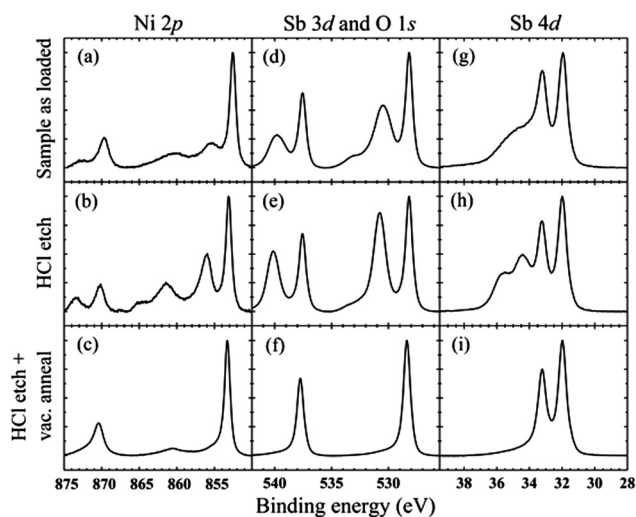
FIG. 8. XPS data for NiSb after different treatments: top row untreated, middle row after wet etching with HCl, and bottom row after subsequent vacuum annealing. The Ni 2p, Sb 3d, O 1s, and Sb 4d regions are shown.

approximately 3.0 eV larger than the main doublet. This is concurrent with the increase in the Sb oxide component. The anneal then removes this peak effectively, which could be assigned to a Ni hydroxide.[52,55] After etch and anneal, Ni 2p region appears as a doublet of asymmetric peaks with the main $2p_{3/2}$ peak at 853.3 eV and a broad feature centered at 860.6 eV. The main peak is closer in binding energy to NiO or Ni intermetallics than to metallic Ni (Refs. 52 and 56) consistent with assignment to NiSb.

For MnSb, the Mn 2p region does not evolve significantly as the surface treatment progresses. The main peak is broad and asymmetric, centered on binding energy 641.8 eV. The spin–orbit splitting Δ_{SO} for first-row transition metal 2p levels varies depending on the local environment and chemical state.[57] Our clean polycrystalline MnSb shows a value $\Delta_{SO} = (11.5 \pm 0.2)$ eV, consistent with a previous determination[58] for MnSb of 11.6 eV. Between these two main spin-orbit-split peaks lies a broad feature at around 646.9 eV, which can be tentatively assigned to a shake-up feature.[58] The spectra for clean NiSb are similar, with $\Delta_{SO} = (17.2 \pm 0.2)$ eV, closer to Ni metal (17.4 eV) or Ni(B,S,P) alloys[59] ($\sim$17.0 eV) than NiO (18.4 eV), in agreement with the direct core level results.

Table II shows the stoichiometry of the materials during preparation. Both binaries are Sb rich after cleaning. The XPS data are consistent with a Sb layer on top of stoichiometric material, as observed previously for MnSb thin films.[37] On both NiSb and MnSb, some C and Cl

TABLE I. Fraction of oxidized Sb inferred from fitting Sb 4d peaks as a function of surface cleaning stage for NiSb, MnSb, and NiMnSb.

Preparation stage	NiSb	MnSb	NiMnSb
Untreated	36	66	52
Etch only	56	18	
10 s etch and anneal	6	3	40
30 s etch and anneal			26
IBA			12

TABLE II. Stoichiometry as a function of surface cleaning for NiSb, MnSb, and NiMnSb.

Preparation stage	[Sb]/[Ni]	[Sb]/[Mn]	Ni:Mn:Sb surface	Ni:Mn:Sb bulk
Untreated	1.4	1.0	0.4:0.5:1	0.8:1.3:1
Etch only	2.5	10.0		
10 s etch and anneal	1.3	1.4		0.7:1.4:1
30 s etch and anneal				0.7:1.4:1
IBA			0.6:1.6:1	0.8:1.3:1

contamination remains after the cleaning process, at levels around 2%–5% of total elemental composition. However, the behavior of the metal, O and Sb peaks indicates that surface cleaning via HCl etch and vacuum anneal is effective for both materials, efficiently removing the surface oxide.

D. Chemical cleaning and argon sputtering of NiMnSb

The ternary compound was studied in a similar manner to the binaries, but with two different etching times. It was also studied separately by IBA. Example XPS data are shown in Figs. 9 and 10. The shallow core regions are shown in Fig.
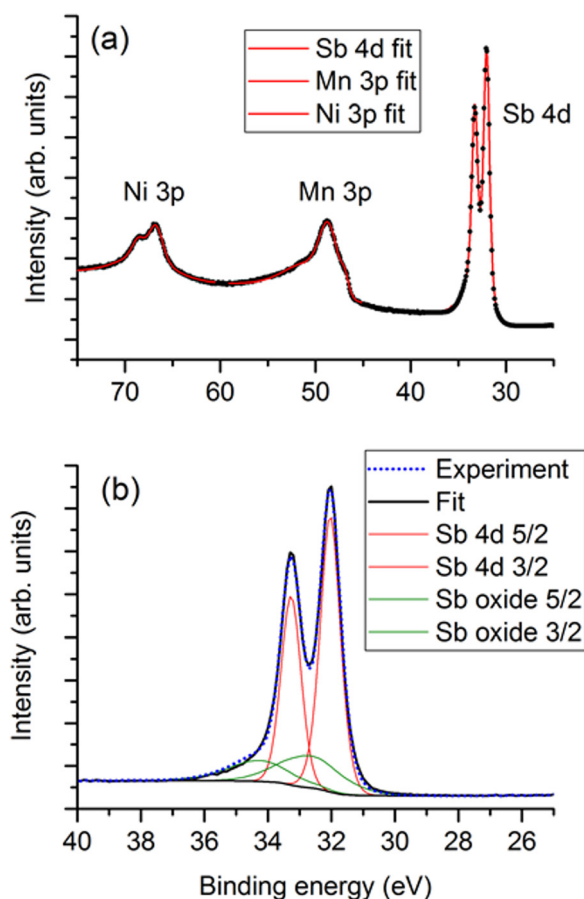

FIG. 9. (Color online) Example shallow-core XPS data and fits for NiMnSb after etch and anneal. Panel (a) shows data (circles) after 10 s acid etch and anneal, with Ni 3p, Mn 3p, and Sb 4d regions fitted (red solid line; components not shown for clarity). Panel (b), after 30 s etch and anneal, shows the Sb 4d peaks (blue dashed line) with two-component fit (black heavy solid line) comprising NiMnSb (red fine solid line, two sharp intense peaks) and Sb oxide (green fine solid line, two broad weak peaks).
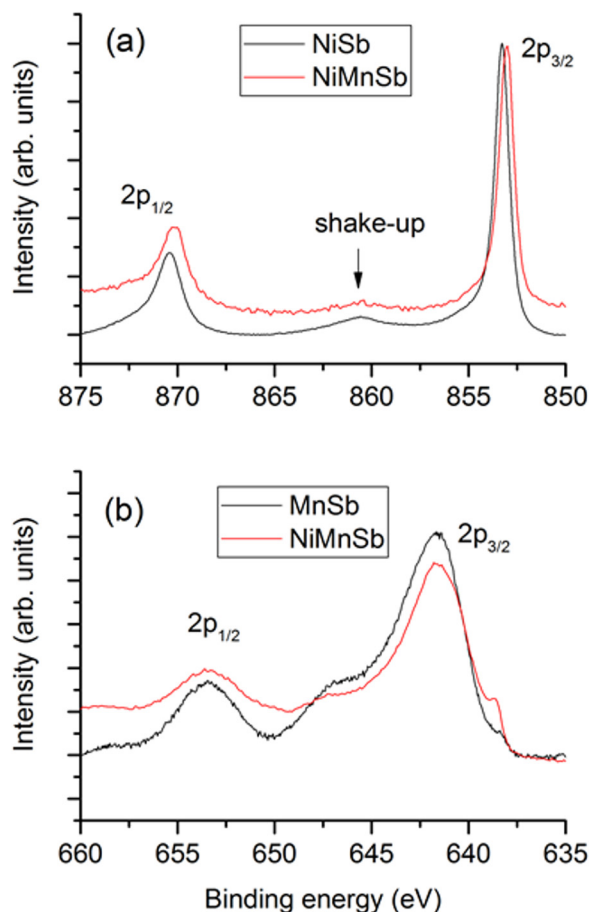
FIG. 10. (Color online) Comparison of transition metal 2p XPS spectra for NiMnSb, NiSb, and MnSb after acid etch and vacuum anneal.

9(a), with well resolved Ni 3p, Mn 3p and Sb 4d core levels. The Ni 3p and Mn 3p regions were readily fitted with standard Shirley background and three Voigt peaks, primarily to obtain peak areas for stoichiometry trend estimation. The peak shapes and areas hardly change between the short and long etch/anneal samples. The main Ni 3p doublet appeared as peaks at binding energy 66.8 and 68.6 eV on a broad background. These can be assigned to the spin–orbit split components of a Ni^{2+} state[56] and the splitting, $\Delta_{SO} \simeq 1.8$ eV, is similar to that found in Ni intermetallics.[60] The Mn region contains a weak feature at low binding energy (46.9 eV) and main peak at 48.6 eV, plus a broad peak at higher binding energy (around 50.6 eV). The main peak can be tentatively assigned to a Mn^{3+} state[56] while the higher binding energy peak may be due to mixed-valence Mn. The small 46.9 eV component is characteristic of metallic Mn.[61]

Turning to the transition metal 2p levels, Fig. 10 compares the NiMnSb, NiSb, and MnSb data. Panel (a) shows superimposed Ni 2p spectra for NiMnSb and NiSb. Although the backgrounds differ somewhat the core level spectra are clearly very similar. Binding energies are very slightly higher for NiSb (by 0.2 eV), but the spin–orbit splitting is nearly identical, as is the position of the broad shake-up feature at (860.6 ± 2) eV. For Ni(S,P,B) alloys,[59] the shake-up intensity has been related to shift of Ni 3d levels relative to the Fermi level as a function of alloying species and fraction, and

consequent probability that the final state of the photoionized Ni atom is $[core^{-1}]3d^{10}4s$ or $[core^{-1}]3d^{9}4s^{2}$. Our values of ~7% of the main peak area for NiMnSb and ~9% for NiSb are broadly consistent with the group V (Ni-P) alloys. Figure 10(b) shows the corresponding data for Mn 2p. Features in the NiMnSb spectrum are generally broader and less clearly resolved than that for MnSb. The spin–orbit splitting is only slightly larger at $\Delta_{SO} = (11.9 \pm 0.2)$ eV. The possible shake-up feature around 647 eV is less prominent than in MnSb and there appears to be more metalliclike Mn present as indicated by the stronger shoulder at 638.6 eV.

The ratio of Sb oxide to Sb in NiMnSb is shown in Table I [derived from Sb 4d analysis, e.g., Fig. 9(b)]. The etch and anneal process is less efficient at reducing the Sb oxide when compared to NiSb or MnSb. The Sb oxides can be removed by IBA but even after several cycles the fraction remains above 10%. The stoichiometry is summarized in Table II. For untreated NiMnSb, the surface appears to be Sb-rich with approximately twice the Sb concentration compared to the transition metals. It is closer to stoichiometry overall when the longer IMFP data (shallow cores) are analyzed, but still strongly Mn-rich compared to Ni.

In Fig. 11, we show the evolution of NiMnSb stoichiometry during a sequence of IBA treatments. An initial anneal causes the Mn surface enrichment to appear rapidly; subsequent treatment then causes a steady increase of Mn surface content (black squares). This surface segregation is observed even in the bulk signal with long IMFP after the final 12 h anneal. In contrast, the Ni signal changes rather little as the treatment proceeds, being strongly deficient in the surface signal and moderately deficient in the bulk. Increasing the ion energy to 1 keV appeared to increase the Mn enrichment: a surface composition ratio as high as Mn:Sb 4:1 appeared after a 30 min IBA cycle with the higher ion energy.
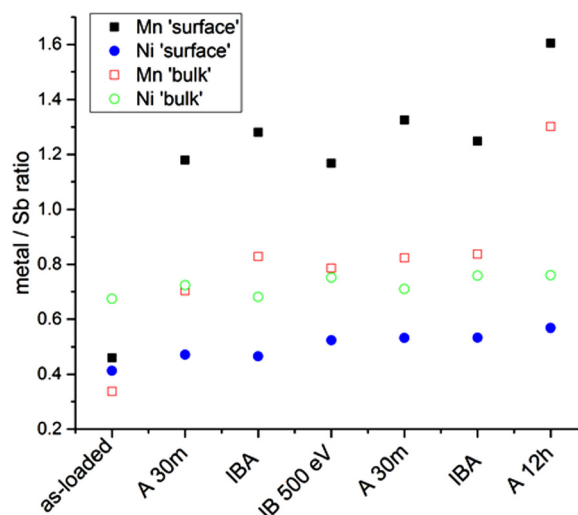

FIG. 11. (Color online) Stoichiometry evolution of NiMnSb during sequential *in vacuo* surface treatment. The labels bulk and surface refer to stoichiometries derived from shallow core levels (Sb 4d, metal 3p) and deeper lying core levels (Sb 3d, metal 2p), respectively, i.e., indicate only the relative depth sensitivity of the XPS measurement. The Mn and Ni concentrations are normalized to that of Sb. The labels refer to 30 min annealing cycles at 300 °C (A 30 m), ion bombardment with 500 eV Ar^{+} for 30 min (IB 500 eV) or both (IBA). The final anneal was 12 h.

E. Discussion

In the present study, HCl etching and annealing alone could prepare oxide-free MnSb and NiSb surfaces with slight Sb excess. It is likely that this is due to residual Sb at the surface, as we found previously for MnSb thin films.[37] These Sb layers can protect samples from native oxide formation (especially Mn oxides) and so the simple HCl etch has proved valuable in, for example, device fabrication and transport measurements with MnSb. We did not detect any nanostructuring effect for our (100) bulk crystals under the conditions employed here as observed by Eickhoff *et al.*[39] for NiMnSb(110). Ristoiu *et al.*[33] studied IBA of NiMnSb(100) films deposited on MgO, reporting a high degree of sensitivity of spin-resolved inverse photoemission measurements to the surface preparation. They found that sputtering enriched the surface with Sb, followed by Mn enrichment on annealing to remove the Sb. The behavior of our bulk samples was somewhat different but retained the trend toward surface enrichment of Mn compared to Ni even prior to cleaning treatment (Table II). This was not improved by extended IBA cycles and it was not possible to achieve stoichiometric NiMnSb by IBA or by HCl etching. It is clear that the simple etch-and-anneal procedure which effectively cleans NiSb and MnSb is far less efficient when applied to NiMnSb. Interestingly, for samples glued to stubs with epoxy resin, curing of the epoxy in air at 200 °C for several hours caused MnSb to discolor significantly (forming a brownish oxide layer) while the NiMnSb retained its shiny silver surface finish. We have not investigated further this thicker oxide layer on MnSb (or NiSb), but the observation does highlight a difference in surface chemistry between the ternary and binary compounds. AHC has been used successfully on III–V semiconductors[38] and is a plausible low-damage route to Heusler alloy surface preparation in combination with chemical etching.

IV. SUMMARY AND CONCLUSIONS

For both bulk crystal growth and surface preparation, the ternary compound NiMnSb behaves somewhat differently from its binary pnictide relations NiSb and MnSb. As expected from its higher vapor pressure, excess Sb is required for bulk crystal growth of stoichiometric binary materials. In agreement with previous work,[3,30] we find that a small excess of Mn is also required to form stoichiometric bulk NiMnSb. The NiMnSb lattice parameter was found to be 5.945 ± 0.001 Å at room temperature, slightly larger than values previously reported. Stoichiometric and nearly oxygen-free surfaces of the binary materials NiSb and MnSb can be prepared by etching in HCl and gentle annealing (300 °C) in UHV, the latter in agreement with our previous studies on epitaxially grown thin films.[37] However, surface oxides appear to be much more stubborn on NiMnSb and a stoichiometric surface could not be prepared by wet etching, annealing and Ar ion sputtering in UHV. The difficulty of NiMnSb surface preparation has been noted by other groups and has probably contributed to varying assessments of its spin polarization. A semiquantitative analysis of the core

level spectra of the three materials after surface cleaning has been given. In terms of both core level shifts and the 2p transition metal spectra (satellite features and spin–orbit splitting), NiMnSb behaves very similarly to its binary counterparts. A more detailed study including valence band data and first-principles calculations will be given in a future paper.

[1]W. Q. Zou *et al.*, J. Magn. Magn. Mater. **321**, 291 (2009).
[2]J. Minár, J. Braun, S. Bornemann, H. Ebert, and M. Donath, J. Phys. D: Appl. Phys. **42**, 084009 (2009).
[3]F. Wang, T. Fukuhara, K. Maezawa, K. Nishimura, F. Shimizu, and S. Masubuchi, Jpn. J. Appl. Phys., Part 1 **49**, 025502 (2010).
[4]P. J. Brown, A. P. Gandy, R. Kainuma, T. Kanomata, T. Miyamoto, M. Nagasako, K. U. Neumann, A. Sheikh, and K. R. A. Ziebeck, J. Phys. Condens. Matter **22**, 206004 (2010).
[5]B. Zhang, J. A. Heuver, F. Wang, J. Baas, G. A. de Wijs, T. Fukuhara, T. T. M. Palstra, and R. A. de Groot, Phys. Rev. B **88**, 014418 (2013).
[6]F. Gerhard, C. Schumacher, C. Gould, and L. W. Molenkamp, J. Appl. Phys. **115**, 094505 (2014).
[7]P. Dürrenfeld, F. Gerhard, M. Ranjbar, C. Gould, L. W. Molenkamp, and J. Åkerman, J. Appl. Phys. **117**, 17E103 (2015).
[8]H. Allmaier, L. Chioncel, E. Arrigoni, M. I. Katsnelson, and A. I. Lichtenstein, Phys. Rev. B **81**, 054422 (2010).
[9]S. V. Eremeev, A. V. Bakulin, and S. E. Kul'kova, Phys. Solid State **52**, 105 (2010).
[10]S. W. Fan, X. P. Huang, L. J. Ding, Z. L. Wang, and K. L. Yao, Comput. Mater. Sci. **82**, 345 (2014).
[11]X.-P. Wei, Y.-D. Chu, X.-W. Sun, Y. E, J.-B. Deng, and Y.-Z. Xing, J. Magn. Magn. Mater. **363**, 55 (2014).
[12]B. Zhou, S. Dong, S. Chen, Z. Zhang, H. Zhao, and P. Wu, Solid State Commun. **192**, 64 (2014).
[13]H.-B. Xu, S.-W. Fan, X.-B. Yang, L.-Q. Pan, and K.-L. Yao, Jpn. J. Appl. Phys., Part 1 **53**, 125801 (2014).
[14]R.-J. Zhang, U. Eckern, and U. Schwingenschlögl, ACS Appl. Mater. Interfaces **6**, 14516 (2014).
[15]Y. Feng, X. Chen, T. Zhou, H. Yuan, and H. Chen, Appl. Surf. Sci. **346**, 1 (2015).
[16]N. Liu, G. Y. Gao, J. B. Liu, and K. L. Yao, Comput. Mater. Sci. **95**, 557 (2014).
[17]Z. Nedelkoski, P. J. Hasnip, A. M. Sanchez, B. Kuerbanjiang, E. Higgins, M. Oogane, A. Hirohata, G. R. Bell, and V. K. Lazarov, Appl. Phys. Lett. **107**, 212404 (2015).
[18]R. A. de Groot and F. M. Mueller, Phys. Rev. Lett. **50**, 2024 (1983).
[19]L. Bainsla, A. I. Mallick, A. A. Coelho, A. K. Nigam, B. S. D. C. S. Varaprasad, Y. K. Takahashi, A. Alam, K. G. Suresh, and K. Hono, J. Magn. Magn. Mater. **394**, 82 (2015).
[20]J. D. Aldous, C. W. Burrows, A. M. Sánchez, R. Beanland, I. Maskery, M. K. Bradley, M. dos Santos Dias, J. B. Staunton, and G. R. Bell, Phys. Rev. B **85**, 060403 (2012).
[21]S. Zhu, J. Liu, Y. Ni, and K. Yao, J. Alloys Compd. **655**, 32 (2016).
[22]M. El Amine Monir, R. Khenata, G. Murtaza, H. Baltache, A. Bouhemadou, Y. Al-Douri, S. Azam, S. Bin Omran, and H. Ud Din, Indian J. Phys. **89**, 1251 (2015).
[23]W.-H. Xie, Y.-Q. Xu, B.-G. Liu, and D. Pettifor, Phys. Rev. Lett. **91**, 037204 (2003).

[24]N. Zu, R. Li, Q. Li, and J. Wang, J. Magn. Magn. Mater. **399**, 72 (2016).

[25]T. Guan et al., Phys. Rev. Lett. **115**, 087002 (2015).

[26]H. K. Singh, P. Kumar, and U. V. Waghmare, J. Phys. Chem. C **119**, 25657 (2015).

[27]R. Skomski and P. A. Dowben, Europhys. Lett. **58**, 544 (2002).

[28]M. I. Katsnelson, V. Y. Irkhin, L. Chioncel, A. I. Lichtenstein, and R. A. de Groot, Rev. Mod. Phys. **80**, 315 (2008).

[29]D. S. Hirashima, J. Phys. Soc. Jpn. **84**, 124707 (2015).

[30]S. Gardelis, J. Appl. Phys. **95**, 8063 (2004).

[31]J. Park, E. Vescovo, H. Kim, C. Kwon, R. Ramesh, and T. Venkatesan, Nature **392**, 794 (1998).

[32]C. M. Fang, G. A. de Wijs, and R. A. de Groot, J. Appl. Phys. **91**, 8340 (2002).

[33]D. Ristoiu, J. P. Nozières, C. N. Borca, T. Komesu, H.-k. Jeong, and P. A. Dowben, Europhys. Lett. **49**, 624 (2000).

[34]G. L. Bona, F. Meier, M. Taborelli, E. Bucher, and P. H. Schmidt, Solid State Commun. **56**, 391 (1985).

[35]M. A. G. Dixon, J. A. Duffy, S. Gardelis, J. E. McCarthy, M. J. Cooper, S. B. Dugdale, T. Jarlborg, and D. N. Timms, J. Phys. Condens. Matter **10**, 2759 (1998).

[36]J. A. Duffy, J. W. Taylor, S. B. Dugdale, C. Shenton-Taylor, M. W. Butchers, S. R. Giblin, M. J. Cooper, Y. Sakurai, and M. Itou, Phys. Rev. B **81**, 134424 (2010).

[37]S. A. Hatfield, J. D. Aldous, and G. R. Bell, Appl. Surf. Sci. **255**, 3567 (2009).

[38]A. Khatiri, J. Ripalda, T. Krzyzewski, G. R. Bell, C. F. McConville, and T. Jones, Surf. Sci. **548**, L1 (2004).

[39]C. Eickhoff, H. Kolev, M. Donath, G. Rangelov, and L. F. Chi, Phys. Rev. B **76**, 205440 (2007).

[40]H. Akinaga, S. Miyanashi, and S. Yoshishige, Jpn. J. Appl. Phys., Part 2 **35**, L897 (1996).

[41]T. Amemiya, Y. Ogawa, H. Shimizu, H. Munekata, and Y. Nakano, Appl. Phys. Express **1**, 022002 (2008).

[42]C. M. Ionica-Bousquet, M. Womes, P.-E. Lippens, J. Olivier-Fourcade, B. Ducourant, and A. V. Chadwick, Hyperfine Interact. **167**, 773 (2006).

[43]J. D. Aldous et al., J. Cryst. Growth **357**, 1 (2012).

[44]C. Villevieille, C. M. Ionica-Bousquet, A. De Benedetti, F. Morato, J. F. Pierson, P. Simon, and L. Monconduit, Solid State Ionics **192**, 298 (2011).

[45]H. Hou, X. Cao, Y. Yang, L. Fang, C. Pan, X. Yang, W. Song, and X. Ji, Chem. Commun. **50**, 8201 (2014).

[46]E. Allcorn and A. Manthiram, J. Phys. Chem. C **118**, 811 (2014).

[47]C. W. Lee, J.-C. Kim, S. Park, H. J. Song, and D.-W. Kim, Nano Energy **15**, 479 (2015).

[48]J. Liu, Z. Yang, J. Wang, L. Gu, J. Maier, and Y. Yu, Nano Energy **16**, 389 (2015).

[49]J. Xie, X. B. Zhao, H. M. Yu, H. Qi, G. S. Cao, and J. P. Tu, J. Alloys Compd. **441**, 231 (2007).

[50]P. P. Shanbogh and S. C. Peter, RSC Adv. **3**, 22887 (2013).

[51]G. Jiang, Y. Chen, T. Zhu, X. Liu, and X. Zhao, J. Mater. Res. **28**, 3394 (2013).

[52]M. C. Biesinger, B. P. Payne, L. W. M. Lau, A. Gerson, and R. S. C. Smart, Surf. Interface Anal. **41**, 324 (2009).

[53]P. J. Webster and R. M. Mankikar, J. Magn. Magn. Mater. **42**, 300 (1984).

[54]P. P. J. van Engelen, D. B. de Mooij, J. H. Wijngaard, and K. H. J. Buschow, J. Magn. Magn. Mater. **130**, 247 (1994).

[55]M. C. Biesinger, B. P. Payne, A. P. Grosvenor, L. W. M. Lau, A. R. Gerson, and R. S. C. Smart, Appl. Surf. Sci. **257**, 2717 (2011).

[56]L. Baggetto, N. J. Dudney, and G. M. Veith, Electrochim. Acta **90**, 135 (2013).

[57]J. Liu, M. P. Hanson, J. A. Peters, and B. W. Wessels, ACS Appl. Mater. Interfaces **7**, 24159 (2015).

[58]B. L. Low, C. K. Ong, J. Lin, A. C. H. Huan, H. Gong, and T. Y. F. Liew, J. Appl. Phys. **85**, 7340 (1999).

[59]S. Diplas and O. M. Løvvik, J. Phys. Condens. Matter **21**, 245503 (2009).

[60]F. U. Hillebrecht, J. C. Fuggle, P. A. Bennett, Z. Zołnierek, and C. Freiburg, Phys. Rev. B **27**, 2179 (1983).

[61]A. R. Chourasia, Surf. Sci. Spectra **3**, 74 (1994).